HHS Public Access

Author manuscript

Neuroimage. Author manuscript; available in PMC 2021 June 23.

Published in final edited form as:

Neuroimage. 2021 May 15; 232: 117897. doi:10.1016/j.neuroimage.2021.117897.

Variable flip angle echo planar time-resolved imaging (vFA-EPTI) for fast high-resolution gradient echo myelin water imaging

Zijing Dong[a,b,*], **Fuyixue Wang**[a,c], **Kwok-Shing Chan**[d], **Timothy G. Reese**[a], **Berkin Bilgic**[a,c], **José P. Marques**[d], **Kawin Setsompop**[a,c]

[a]Athinoula A. Martinos Center for Biomedical Imaging, Massachusetts General Hospital, Charlestown, Massachusetts, USA [b]Department of Electrical Engineering and Computer Science, MIT, Cambridge, Massachusetts, USA [c]Harvard-MIT Health Sciences and Technology, MIT, Cambridge, Massachusetts, USA [d]Donders Institute for Brain, Cognition and Behaviour, Radboud University, Nijmegen, Netherlands

Abstract

Myelin water imaging techniques based on multi-compartment relaxometry have been developed as an important tool to measure myelin concentration in vivo, but are limited by the long scan time of multi-contrast multi-echo acquisition. In this work, a fast imaging technique, termed variable flip angle Echo Planar Time-Resolved Imaging (vFA-EPTI), is developed to acquire multi-echo and multi-flip-angle gradient-echo data with significantly reduced acquisition time, providing rich information for multi-compartment analysis of gradient-echo myelin water imaging (GRE-MWI). The proposed vFA-EPTI method achieved 26 folds acceleration with good accuracy by utilizing an efficient continuous readout, optimized spatiotemporal encoding across echoes and flip angles, as well as a joint subspace reconstruction. An approach to estimate off-resonance field changes between different flip-angle acquisitions was also developed to ensure high-quality joint reconstruction across flip angles. The accuracy of myelin water fraction (MWF) estimate under high acceleration was first validated by a retrospective undersampling experiment using a lengthy fully-sampled data as reference. Prospective experiments were then performed where whole-brain MWF and multi-compartment quantitative maps were obtained in 5 min at 1.5 mm isotropic resolution and 24 min at 1 mm isotropic resolution at 3T. Additionally, ultra-high resolution data at 600 μm isotropic resolution were acquired at 7T, which show detailed structures within the

*Corresponding author. zijingd@mit.edu (Z. Dong).

Credit authorship contribution statement

Zijing Dong: Conceptualization, Methodology, Software, Validation, Writing – original draft, Writing – review & editing, Visualization. **Fuyixue Wang:** Methodology, Software, Validation, Writing – review & editing. **Kwok-Shing Chan:** Software, Validation, Writing – review & editing. **Timothy G. Reese:** Methodology, Software. **Berkin Bilgic:** Software, Writing – review & editing. **José P. Marques:** Writing – review & editing, Supervision, Funding acquisition. **Kawin Setsompop:** Conceptualization, Writing – review & editing, Supervision, Funding acquisition.

7. Data and code availability statement

The example codes of the proposed reconstruction, example raw data, and main results have been made publicly available, which can be download at https://github.com/zijingd/VFA-EPTI and https://figshare.com/articles/dataset/VFA-EPTI_Datasets/13211669.

Supplementary materials

Supplementary material associated with this article can be found, in the online version, at doi:10.1016/j.neuroimage.2021.117897.

cortex such as the line of Gennari, demonstrating the ability of the proposed method for submillimeter GRE-MWI that can be used to study cortical myeloarchitecture *in vivo*.

Keywords

Myelin water imaging; Fast imaging; High resolution; Multi-compartment; Myeloarchitecture; Cortical layers

1. Introduction

Myelin is a membrane structure around nerve fibers that enables efficient conduction of action potential (Hildebrand et al., 1993). Myelination is an important process for brain development (Wang et al., 2009), and demyelination is associated with many neurodegenerative disorders such as multiple sclerosis (Filippi et al., 2016). Therefore, studies of myeloarchitecture of the human brain could help us gain further understanding of its functional organization (Amunts and Zilles, 2015; Paus, 2018).

There has been a strong interest in the development of non-invasive methods to measure the myelin content in the human brain. MRI myelin water fraction imaging (MWI) (Mackay et al., 1994) provides an important non-invasive tool to measure *in vivo* myelin water content, which has been demonstrated to have good correlation with histopathological myelin measurement (Laule et al., 2008; Laule et al., 2006; Webb et al., 2003). MWI is conventionally performed using multi-echo spin-echo sequence and multi-compartment modeling to analyze the myelin water concentration based on different T_2 relaxation times of myelin and other tissue compartments (Mackay et al., 1994). As an alternative approach to multi-echo spin-echo approach, multi-echo gradient-echo sequence with multi-compartment T_2* decay analysis has been proposed (GRE-MWI) (Du et al., 2007) and demonstrated to provide a myelin water measurement that is in good agreement with the spin-echo approach (Alonso-Ortiz et al., 2018). In comparison to the conventional approach, the GRE-based method achieves lower specific absorption rate (SAR) and higher data acquisition efficiency by avoiding the use of refocusing pulses. These advantages allow GRE-MWI to achieve higher isotropic spatial resolution in a reduced timeframe and to be more applicable at ultra-high field systems (e.g., 7T) (Shin et al., 2019).

A number of refinements has been made to GRE-MWI in recent years, including the use of a complex-value signal model for improved multi-compartment T_2* analysis (Nam et al., 2015b; Sati et al., 2013; van Gelderen et al., 2012), B_0 field inhomogeneity correction to compensate for signal dephasing (Alonso-Ortiz et al., 2017; Lee et al., 2018a), and physiological noise correction to address the respiration induced phase errors (Nam et al., 2015a). To further improve the accuracy of myelin water fraction (MWF) estimate, an extended complex-value GRE-MWI model was recently developed (Chan and Marques, 2019; Chan and Marques, 2020). In this approach, multi-echo GRE datasets are acquired with variable flip angles (vFA), where the added T_1 sensitivity can be used for better signal separation and to avoid the overestimation of MWF, since myelin water has a shorter T_1 than other water components. Even though the quality of myelin water imaging is significantly improved by these recent developments, the slow imaging speed due to the requirements of

high SNR and multi-echo acquisition for multi-compartment analysis still remains a major challenge. The T_1-corrected GRE-MWI with vFA acquisition improves the conditioning of myelin estimation Chan and Marques (2020), but further prolongs the acquisition time. The slow acquisition of MWI limits the achievable spatial resolution and its application in both clinical and neuroscience research. Currently, GRE-MWI is typically performed at a relatively low spatial resolution of 1.5 mm to 2 mm (Lee et al., 2018b; Shin et al., 2019). Such resolution is not adequate for the analysis of myelination within the cortex, hence, in-vivo studies of cortical myeloarchitecture have so far been limited to the use of single-compartment quantitative model or contrast-weighted images (Glasser and Van Essen, 2011; Haast et al., 2016; Lutti et al., 2014; Marques and Gruetter, 2013; Marques et al., 2017; Weiskopf et al., 2015).

Echo planar time-resolved imaging (EPTI) (Dong et al., 2019; Wang et al., 2019a) is an efficient multi-shot EPI acquisition technique for multi-contrast and quantitative imaging, which not only achieves distortion- and blurring-free imaging, but also resolves hundreds of T_2/T_2*-weighted images across the EPI readout. The recent extension of EPTI to 3D volumetric encoding with 3D-EPTI (Dong et al., 2020; Wang et al., 2019b) further improves its acquisition efficiency for multi-parametric quantitative mapping at high spatial resolution. In this study, we developed a novel imaging technique based on 3D-EPTI, termed variable flip angle EPTI (vFA-EPTI), in order to acquire multi-echo and multi-flip-angle GRE-MWI data with significantly reduced acquisition time. To enable good reconstruction performance and SNR at very high accelerations, a new spatiotemporal sampling strategy and a joint subspace reconstruction for multi-echo multi-FA acquisition were developed. The extended complex 3-compartment model for myelin water fraction imaging with T_1 correction Chan and Marques (2020) was utilized for MWF estimation. Enabled by the high acceleration achieved using the proposed method, whole-brain MWF, proton density (PD), and multi-compartment T_1 & T_2* maps can be acquired simultaneously in 5 min at 1.5 mm isotropic resolution and in 24 min at 1 mm isotropic resolution at 3T. Moreover, a 600 μm isotropic dataset was also acquired at 7T to demonstrate the ability of the proposed method for cortical myelination analysis.

The example codes of reconstruction and representative results have been made publicly available, which can be download at https://github.com/zijingd/VFA-EPTI and https://figshare.com/articles/dataset/VFA-EPTI_Datasets/13211669.

2. Material and methods

2.1. 3D vFA-EPTI acquisition

A 3D gradient-echo (GE) EPTI acquisition (Dong et al., 2020) is used to acquire multi-echo T_2*-weighted images with high acquisition efficiency. Fig. 1A shows the sequence diagram of the 3D GE-EPTI acquisition. After each excitation pulse, a continuous 3D-EPTI readout is performed with multiple phase-encoding (PE) lines, where each PE line is represented by a filled circle in the k_y-k_z-t space as illustrated in the bottom-left plot. Within each TR, a large block of k_y-k_z encoding is acquired using a highly under-sampled spatiotemporal CAIPI encoding pattern that allows the missing data to be effectively recovered by taking advantage of both coil sensitivity and temporal correlation between signals (Dong et al.,

2020; Wang et al., 2019a). Such k_y-k_z block encoding with EPI readout provides a high gain in acquisition efficiency than standard multi-echo GRE acquisition, where a single k_y-k_z encoding is repeatedly acquired across the echoes in each TR. The bottom-right of Fig. 1A shows the block sampling of EPTI in k_y-k_z space, where different blocks are sampled across TRs to fill the full 3D k-space.

To improve the reconstruction performance at high accelerations (i.e., larger k_y-k_z block sizes), a temporal-variant spatiotemporal CAIPI encoding is implemented (Fig. 1B), where different echo sections within each EPTI readout are encoded with different CAIPI patterns to provide complementary *k*-space information (Dong et al., 2020). For the proposed variable flip angle 3D GE-EPTI sequence, the complementary *k*-*t* encoding strategy is further extended across flip angles (Fig. 1C) to improve the performance. Since the T_2* decay of myelin water is very short, the minimum echo times (TE) are reduced by using non-selective excitation pulses. To estimate the coil sensitivity and an initial off-resonance map (B_0 map) for image reconstruction, a low-resolution *k*-*t* calibration dataset is also acquired only once before the first FA acquisition.

2.2. Multi-compartment relaxometry model (MCR)

The multi-compartment relaxometry (MCR) model Chan and Marques (2020) which extends the complex-value 3-compartment GRE-MWI model (Nam et al., 2015b; van Gelderen et al., 2012) to account for the multi-compartment T_1 effect, is used as a representative application of the proposed acquisition method. In the standard complex-value GRE-MWI model, three water pools: myelin water (MW), axon water (AX) and extracellular water (EX), have three different amplitudes (A), T_2*, and frequency offsets (ω), which can be represented by (Nam et al., 2015b):

$$S(t) = \left(A_{MW}e^{i\omega_{MW}t}e^{-t/T^*_{2,MW}} + A_{AX}e^{i\omega_{AX}t}e^{-1/T^*_{2,AX}} + A_{EX}e^{i\omega_{EX}t}e^{-1/T^*_{2,EX}}\right)e^{i(\omega_b t+\theta)}, \quad (1)$$

where ω_b is the background off-resonance frequency, and θ is the initial background phase.

To correct for the multi-compartment T_1-weighting effect, the T_1 of different water pools can be estimated from the vFA acquisition. The steady-state signal of a spoiled GRE sequence for a single pool is:

$$A = M_0 \sin\alpha \frac{1-e^{-TR/T_1}}{1-\cos\alpha e^{-TR/T_1}}, \quad (2)$$

where M_0 is the proton density of the water and α is the flip angle. To estimate multi-compartment T_1 relaxation, axon water and extracellular water are assumed to have the same T_1 in each voxel based on the observation (Chan and Marques, 2020; Oh et al., 2013), with myelin water having a relatively shorter T_1 value. Thus, two pools are assumed in the longitudinal relaxation model: the free water (axon and extracellular water) pool and the myelin sheath pool. An extended phase graph method for systems with magnetization

transfer and exchange (Malik et al., 2018) is also included in the model to account for the effect of inter-compartment magnetization exchange in Eq. 2. The full formalisms of the MCR and the Bloch-McConnell equations governing the longitudinal magnetization can be found in Chan and Marques (2020).

2.3. Joint subspace reconstruction with multi-compartment modeling

To reconstruct the highly-undersampled multi-echo multi-FA data acquired by 3D vFA-EPTI acquisition, a joint subspace reconstruction framework is developed in this study. The low-rank subspace method Liang (2007) is a powerful approach that has enabled good reconstruction for highly undersampled *k-t* data across a number of MR applications (Dong et al., 2020; Guo et al., 2019; Guo et al., 2020; Lam and Liang, 2014; Meng et al., 2020; Peng et al., 2018; Tamir et al., 2019). The subspace approach has also been used to obtain simultaneous acquisition of metabolites, myelin water fraction and tissue susceptibility recently (Li et al., 2019). The main advantage of the subspace approaches for multi-contrast image reconstruction is that the number of unknowns is significantly reduced by using the prior knowledge of the low-rank property of signal evolutions, and higher acceleration and improved SNR can therefore be achieved. The subspace method is also relatively robust to partial volume and multi-compartment effects compared with strict model-based approaches (Dong et al., 2018a; Sumpf et al., 2011). In this work, we extend the concept of subspace reconstruction to 3D vFA-EPTI with the goal of achieving fast and robust high-resolution myelin water imaging. In order to improve the accuracy of myelin water estimation, the MCR model is incorporated in the subspace reconstruction to preserve the complex multi-compartment signal evolution.

As shown in Fig. 2, the complex signal evolutions across different FAs and TEs are simulated based on the MCR model with a wide tissue-parameter range, including proton densities, T_2*, frequency offsets and T_1 of different pools as well as B_1. Temporal subspace bases (ϕ) are then extracted from the simulated signals through principal component analysis (PCA). Then, instead of estimating all the multi-echo images, the coefficient maps of bases (c) are estimated in the subspace reconstruction by (Dong et al., 2020):

$$\min_{c} \| U\ F\ S\ B\phi_c - y \|_2^2 + \lambda R(c)\,. \tag{3}$$

Here, B is the background phase evolution across different echoes and FAs, including the initial background phase and the phase caused by the B_0 inhomogeneity, which is estimated for each FA described below. S denotes the coil sensitivity, F represents the Fourier transform, U is the undersampling mask, and y is the acquired EPTI signals in k-space. $R(c)$ is the locally low-rank regularization of coefficients to further improve the SNR, and λ is the control parameter of the regularization. After solving c, all the images can be generated by ϕc. In this work, 18 subspace bases were selected which can represent the full simulated signal space with an error < 0.5% to ensure accurate recovery of the multi-compartment signals. After reconstructing the complex signal evolutions, multiple quantitative parameters can be estimated using the MCR model, including MWF, multi-compartment PD, T_1 and T_2*.

To ensure accurate joint reconstruction across FAs, background B_0 field changes across different FA acquisitions (due to e.g. drifts) which act to modify the complex signal evolution are incorporated into the reconstruction. To estimate this B_0 field changes, an initial subspace reconstruction is performed for each of the FA acquisitions. In this initial reconstruction, the background B_0 changes between −50 to 50 Hz are simulated in the basis generation, allowing the extracted bases to represent this range of B_0 phase change across echoes. The low-resolution B_0 map estimated from the calibration data is used in the reconstruction, and updated high-resolution B_0 maps can be obtained after this initial reconstruction by a linear fitting of the image phase. The subspace-based B_0 estimation provides faster computation than the previously developed phase-cycling B_0-estimation method (Dong et al., 2020; Ong et al., 2018) by avoiding iteratively updating magnitude and phase. Since the aim of this step is to estimate an accurate background B_0, monoexponential signal model with T_2* decay and B_0 phase change is used to limit the increase in the number of subspace bases due to additional B_0 phase modeling. Moreover, since the T_1 modeling is not needed in this reconstruction for single FA datasets, only 6 bases were used which can represent the T_2* decay and changed B_0 phases with an error < 1%.

2.4. Data acquisition

All data were acquired with a consented institutionally approved protocol, and each experiment was performed with a single subject (N=1). All the 3T experiments were implemented on a Siemens Prisma 3T scanner with a 32-channel head coil (Siemens Healthineers, Erlangen, Germany), and the 7T experiment was conducted on a Siemens Magnetom Terra 7T scanner (Siemens Healthineers, Erlangen, Germany) using 32-channel phased array receive coil with a single RF transmission channel (Nova Medical, Wilmington, MA). Non-selective Gaussian excitation pulse was utilized to shorten the minimum TE and reduce SAR. The readout gradient was applied along the head-foot (HF) direction. Spectrally-selective fat suppression was used for all the experiments to suppress the fat signal. For each experiment, a B_1 map was acquired using a turbo flash (TFL) sequence, which took about 1 min at 2.25 × 2.25 × 3 mm^3 resolution whole brain. The resulting B_1 map was fitted by a 5^{th}-order 3D polynomial function to remove residual anatomical features and then employed for B_1 correction in the fitting process of the GRE-MWI model. Head motion was restrained using foam pillows in all the experiments. Since the imaging protocols were targeting at different acceleration factors and spatial resolutions, their encoding patterns were not the same. The key parameters of the acquisition are illustrated below, and more details of the encoding patterns can be found at https://github.com/zijingd/VFA-EPTI, where encoding patterns of all the experiments and example MATLAB codes to generate the *k-t* encoding are provided.

Experiment 1. : *2.4 mm retrospective undersampling experiment at 3T*—Fully-sampled multi-echo multi-FA 3D GRE data were acquired to evaluate the accuracy of the proposed vFA-EPTI technique by comparing the reconstruction results from retrospectively undersampled data to the fully-sampled reference. The acquisition parameters were: FOV = 212 × 174 × 224 mm^3 (Anterior-Posterior (AP), Left-Right (LR), HF), matrix size = 88 ×72 ×94 (k_y – k_z – k_x), TE range = 1.5 ms–32.7 ms, echo spacing (ESP) = 0.52 ms, number of

echoes = 61, TR = 47 ms, 8 flip angles were acquired (5°, 10°, 15°, 20°, 25°, 30°, 35°, 40°, same for all the experiments), and the total acquisition time was 40 min.

Using this data, synthesized vFA-EPTI data were generated through retrospectively undersampling the *k-t* space by a reduction factor of 26 × using the temporal-variant *k-t* CAIPI sampling pattern. Here, $R = 26\times$ was achieved by a variable density sampling pattern to increase SNR efficiency, where the central region of *k*-space (40 k_y × 32 k_z) was undersampled at $R = 16$ and the outer region at $R = 32$. Furthermore, to provide comparison to the current state-of-the-art approach, an additional undersampled dataset was generated using a 2D CAIPI sampling pattern and reconstructed by SPIRiT reconstruction Lustig and Pauly (2010). Here, a lower acceleration factor of 8 ($R = R_y \times R_z$ 4 × 2) was used to ensure good reconstruction performance.

To evaluate the performance of the proposed method, the reconstructed images as well as the derived quantitative maps were compared against those obtained from the fully-sampled dataset. Additionally, for the vFA-EPTI, the improvements in MWF estimate through the use of (i) multi-compartment modeling in the subspace reconstruction, (ii) complementary sampling across different FAs, (iii) joint subspace reconstruction, were evaluated in further details using fully-sampled dataset as the gold standard. Here, the MWF estimated from the joint subspace reconstruction with multi-compartment bases and complementary sampling was compared with the estimates from using (i) single-compartment subspace bases, (ii) identical sampling across FAs, and (iii) separate subspace reconstruction for each FA, respectively.

2.4.1. Experiment 2: 1.5-mm acquisition at 3T—A 5-minute vFA-EPTI protocol at 1.5 mm isotropic resolution was designed targeting at potential clinical use. A validation dataset was acquired using the following parameters: FOV = 216 × 174 × 216 mm^3, matrix size = 144 × 116 × 144, TE range = 1.3 ms–35.1 ms, ESP = 0.72 ms, number of echoes = 48, TR = 50 ms, number of dummy TRs for each FA = 20, and reduction factor = 26 ($R = 16$ for central 72-k_y × 60-k_z, $R = 32$ for outer k-space). The acquisition time for each FA was 34 s, and the total acquisition time was ~5 min for 8 FAs, which includes the time for a short calibration scan. The low-resolution calibration data were acquired with the same FOV and ESP to obtain the coil sensitivity and an initial estimation of B_0 maps. To accelerate the acquisition of the calibration data, the outer k-space was undersampled and reconstructed using the fully sampled k-space center. The key acquisition parameters of the calibration data were: matrix size = 48 × 36 × 144, fully-sampled *k*-space center region = 12 × 12 × 144, acceleration factor along k_y and k_z at outer k-space = 2 × 2, number of echoes = 8, and TR = 20 ms. The net acceleration factors of k_y and k_z were 1.6 and 1.5 respectively. The total acquisition time for the calibration data was 14.4 s.

2.4.2. Experiment 3: 1-mm acquisition at 3T—1-mm isotropic resolution data were acquired to evaluate the performance of the proposed method for high-resolution MWI at 3T. The acquisition parameters were: FOV = 210 × 176 × 210 mm^3, matrix size = 208 × 172 × 210, TE range = 1.6 ms–53.7 ms, ESP = 0.93 ms, number of echoes = 57, TR = 69 ms, number of dummy TRs for each FA = 20. A smaller acceleration factor of 13 ($R = 8$ for central 96-k_y × 84-k_z, $R = 16$ for outer k-space) was used to increase the SNR for this high-

resolution scan. The acquisition time for each FA was 3 min, and the same 8 FAs were acquired, resulting in a total acquisition time of 24 min. A calibration dataset was also acquired in 18 s: TR = 25 ms, matrix size = 48 × 36 × 210, and the undersampling parameters were the same as those for the 1.5 mm data.

2.4.3. Experiment 4: 600-μm acquisition at 7T—Ultra-high-resolution data were acquired at 600 μm isotropic resolution using vFA-EPTI to validate the ability of the proposed method for high-resolution GRE-MWI at 7T. This dataset was acquired with the following parameters: FOV = 210 × 173 × 210 mm^3, matrix size = 352 × 284 × 350, TE range = 2 ms–52.4 ms, ESP = 1.2 ms, number of echoes = 42, TR = 65 ms, dummy TRs for each FA = 30. A reduction factor of 13 was used to improve SNR (R = 8 for central 168-k_y × 136-k_z, R = 16 for outer k-space). The acquisition time for each FA was 8 minutes and 22 s, and the total acquisition time was 67 min. The additional acquisition time for the calibration data was 1 min 40 s, where 7 echoes were acquired with TR = 21 ms. Other key parameters of the calibration scan were: matrix size = 134 × 96 × 350, and the net acceleration factors of k_y and k_z = 1.7 and 1.6.

In addition to performing multi-compartment reconstruction and analysis on this data, single-pool reconstruction and analysis for T_1 and T_2* relaxation was also performed to assess the feasibility of using vFA-EPTI for fast single-pool quantitative mapping. With the single-pool model, the number of basis needed to provide good signal representation in the subspace reconstruction is 7, which is much lower than the 18 needed in the multi-compartment model. This enables the use of only 3 FAs (10°, 20°, 35°) for single-pool reconstruction, corresponding to a total scan time of ~25 min.

2.5. Data processing and analysis—For image reconstruction, first, the phase difference between odd and even echoes in the raw k-space data was corrected by a linear phase correction similar to ghost correction in EPI. The parameters for this linear phase correction were calculated from the multi-echo central k-space signals in the calibration data. Subsequently, the subspace reconstruction was applied to recover the multi-echo multi-FA images from the highly-undersampled data. The subspace reconstruction was performed using the alternating direction method of multipliers (ADMM) algorithm (Boyd et al., 2011), with a stop criterion in a maximum iteration = 60. After this reconstruction, a local subvoxel-shifts method (Kellner et al., 2016) was applied to mitigate the Gibbs ringing artifacts of the reconstructed images, except for the 7T submillimeter high-resolution experiment in consideration of avoiding potential blurring. The MWF and quantitative multi-compartment parameters, including PD, T_2*, T_1 and frequency offsets of different water pools, were estimated in all the experiments using the MCR model with B_1 correction, which is available at https://github.com/kschan0214/mwi.git (Chan and Marques, 2020). All data processing was performed using MATLAB (MathWorks, Natick, MA).

For the high resolution 7T dataset, cortical surface analysis was also performed to investigate the myeloarchitecture within the cortex. Cortical surfaces of the gray-white matter border and GM-CSF border were estimated using FreeSurfer Fischl (2012) with the recon-all pipeline on the synthetic T_1-weighted images. The synthetic T_1-weighted images were generated using a T_1 map obtained through a single pool fitting of the same vFA data,

so there is no spatial mismatch between the derived quantitative parameters and the extracted surface segmentations. FreeSurfer was used to generate ten intermediate intra-cortical surfaces, which were then applied to MWF and T_1 maps to investigate cortical profiles across different depths.

3. Results

The performance of vFA-EPTI was first evaluated through the 2.4 mm retrospective undersampling experiment at 3T (Experiment 1). Fig. 3a shows the results of the estimated background B_0 changes across the different FA acquisitions, obtained through an initial subspace reconstruction. The image on the top row is the B_0 map from the first flip-angle acquisition at FA = 5°. The B_0 changes (relative to the B_0 map at FA = 5°) calculated from fully-sampled data of the subsequent FA acquisitions are shown in the second row as the reference, and the estimated B_0 changes from the 26 × retrospectively undersampled EPTI data are shown in the third row. The difference maps shown in the fourth row demonstrate the high accuracy of the estimated B_0 changes for all FAs, which validates the effectiveness of the initial B_0 estimation using the subspace method. By correcting the B_0 changes in the joint subspace reconstruction, higher accuracy of MWF estimation was achieved as shown in Fig. 3b. Fig. 4 shows a comparison of the fully-sampled data and the vFA-EPTI data reconstructed using joint subspace reconstruction at $R = 26$, without Gibbs ringing artifacts correction. The reconstructions of the fully-sampled data (first row) and the EPTI (second row) are almost identical, with small differences in both magnitude (third row) and phase (third row) across the images at different FAs and TEs, presumably originated from noise and Gibbs ringing. The Gibbs ringing artifacts are less prominent in the EPTI images due to the effect of the locally-low rank constraint in the subspace reconstruction. By using vFA-EPTI method with an acceleration factor of 26, the acquisition time can be reduced from 40 min to 1 min and 32 s.

Fig. 5 shows high consistency of the estimated quantitative parameters in the MCR model calculated from the fully-sampled images (top row) with those from the reconstructed images using vFA-EPTI (second row). The difference maps of the quantitative parameters between vFA-EPTI and the fully sampled data, and between the 2D CAIPI undersampling with SPIRiT reconstruction and the fully-sampled data are also shown in the third and fourth row respectively. Smaller differences are observed using vFA-EPTI despite being 3 × higher in acceleration when compared to the 2D CAIPI case, with mean percentage error (MPE) 10.2% ± 7.6% vs. 15.0% ± 10.6%. In addition, Fig. S1 in the Supplementary Information shows the estimated MWF maps from the proposed method (second column), joint reconstruction with single-compartment subspace bases (third column), identical sampling across FAs (forth column), and separate subspace reconstruction for each FA (fifth column). Larger errors are shown in the cases of single-pool basis (MPE = 12.8% ± 10.0%), identical sampling (MPE = 13.0% ± 11.4%), and separate subspace reconstruction (MPE = 12.9% ± 10.0%) (yellow arrows), demonstrating that the advantages of using complex model, complementary sampling and joint reconstruction in the proposed method in improving the accuracy of MWF estimation (MPE = 10.2% ± 7.6%).

The estimated MWF and multi-compartment quantitative parameters of the 5 min 1.5 mm isotropic acquisition (Experiment 2) using vFA-EPTI at $R = 26$ is shown in Fig. 6. The estimated MWF in the white-matter areas are of relatively higher values when compared to the gray matter areas as expected. Moreover, the highly-myelinated fiber bundles including the cingulum, genu and splenium of corpus callosum, corona radiata and optic radiation (red arrows) can be observed in the MWF maps, which demonstrates the ability of this fast protocol to obtain reliable MWF maps. An ROI analysis of MWF is provided in Table S1, which shows consistent values with the previous literature that utilized a multi-gradient-echo acquisition with T_1 correction (Chan and Marques, 2020), and lower values than previous GRE-MWI studies without T_1 correction (Alonso-Ortiz et al., 2018; Shin et al., 2019). Additional analysis of the multi-compartment fitting including the fitted and raw signal evolutions, and MWF estimation using different number of echoes are provided in Fig. S2.

Fig. 7 shows the axial and sagittal views of the estimated MWF, T_1 of free water, T_2* of axon water and total proton density obtained from the 1 mm isotropic acquisition at 3T, with $R = 13$ (Experiment 3) The total acquisition time across the 8 FAs was 24 min, with whole-brain coverage. All the estimated quantitative maps show good image quality, with improved delineation of the fiber bundles in the MWF maps when compared to the 1.5 mm dataset due to the increased resolution. The estimated T_1 map of free water also presents with clearer gray-white mater boundaries at this resolution.

The ultra-high-resolution data were acquired at 600 μm isotropic resolution at 7T using vFA-EPTI (Experiment 4) to validate its potential for submillimeter MWI. As can be seen in Fig. 8, the B_0 off-resonance at 7T is much larger than at 3T, and the B_0 changes across the different FA acquisitions are also larger as reflected by the estimated B_0 changes obtained from the initial subspace reconstruction (Fig. 8 bottom row). The dataset acquired later also shows a larger change than the dataset acquired earlier (e.g., FA 30° vs. FA 10°). The top row of Fig. 8 shows the reconstructed images from a joint subspace reconstruction that has not incorporated in these B_0 changes, where image artifacts and signal dropout can be observed in areas of large B_0 changes in the anterior part of the brain (zoomed-in areas, yellow arrows). With the incorporation of the B_0 changes into the joint subspace reconstruction, these artifacts are well mitigated as shown in the second row of Fig. 8.

Fig. 9a shows the quantitative maps estimated by multi-compartment analysis using 8 FAs at 600 μm isotropic resolution, and more MWF images are shown in Fig. S3. Fig. 9b shows the quantitative T_1 and T_2* maps that were obtained from the single pool reconstruction and analysis using data from only 3 FAs, where the maps show good quality and high SNR. The T_1 map is used to synthesize a T_1-weighted image for surface extraction, and the surface segmentation was then applied to the multi-compartment quantitative maps for analysis (Fig. 9c). Fig. 10b&c zooms in on the T_1 and MWF maps in the calcarine sulcus area (dashed square in Fig. 10a). In the T_1 map, the line of Gennari can be seen as hypo-intense bands around the central cortical depth (red arrows). The line of Gennari is also visible in the MWF map as green bands with higher values (red arrows), however, they are less well-defined due to the limited SNR of the MWF at this ultra-high resolution. The values of T_1 and MWF across different cortical depths at a sampled area depicted by the red circle in Fig. 10b are plotted in Fig. 10d&e, showing a decrease in T_1 and an increase in MWF around the

central depth of the cortex (blue window) as expected from the higher myelination in the line of Gennari. The same cortical depth analysis was also performed in the motor cortex area, the results of which are shown in Fig. S4. Here a relatively homogeneous T_1 and continuously decreasing MWF across the central cortical depth are observed. These observations demonstrate the ability of using EPTI at submillimeter resolution to study myeloarchitecture within the cortex.

4. Discussion

The proposed vFA-EPTI acquisition with joint subspace reconstruction achieved fast acquisition of multi-echo multi-FA GRE data for GRE-MWI and multi-compartment analysis. The retrospective undersampling experiment demonstrated the accurate estimation of MWF and other quantitative maps using vFA-EPTI at a high undersampling rate of 26 ×. Several in-vivo experiments were performed under different spatial resolutions targeting at different applications: the 5 min protocol at 1.5 mm isotropic resolution at 3T aims at clinical use to study demyelinating diseases, the 24 min protocol at 1 mm isotropic resolution at 3T and the 1 h protocol at 600 μm isotropic resolution at 7T are designed for studying myeloarchitecture of the brain *in vivo*. All of these vFA-EPTI protocols were able to produce high quality whole brain MWF maps, with clear white matter bundles, while achieving significant scan time reduction and/or increased spatial resolution. Only a limited number of subjects have been scanned in this preliminary study to evaluate the performance of the method, and more scans and repeatability tests (Hanspach et al., 2021) will need to be conducted for further validation.

The increased efficiency and reduced scan time of vFA-EPTI are achieved by taking advantage of continuous readout, spatial-temporal CAIPI encoding, and improved conditioning of joint subspace reconstruction. The selection of flip angles in this study is not optimized, and further optimization would further improve the SNR of MWF estimation. In addition, incorporation of approaches to improve B_1 homogeneity at 7T, and employment of additional constraints in the reconstruction could also provide further improvements. An example of valid constraints that have been demonstrated, but not explored in this manuscript, is the addition of diffusion information and advanced modelling (Chan and Marques, 2020). This could have a particularly large impact on the higher resolution protocols, and would benefit from some of our recent developments in high-resolution diffusion imaging (Setsompop et al., 2018; Wang et al., 2018). In the subspace reconstruction, using less bases can reduce the number of unknowns and improve the image SNR. However, this could also lead to loss of information if the selected bases cannot fully represent the signal space. In this study, 18 bases were selected that could represent the full simulated signal space with an error < 0.5% and provide a good balance between the accuracy and the SNR. For the single-pool analysis, the model used in bases generation is simplified, and the number of bases can be reduced (e.g., 7 instead 18 bases) to improve the image SNR.

The proposed initial B_0 estimation is an important step to improve the image quality especially at 7T where the B_0 variation is much larger. The results in Fig. 3 and 8 demonstrated the effectiveness of the proposed B_0 estimation and correction. Physiological

noise correction within each FA acquisition could be applied to further improve the image quality and accuracy of the quantitative analysis (Nam et al., 2015a). The significant acceleration introduced by EPTI inherently reduces the sensitivity of MWI to subject motion, but it could still be challenging for high-resolution acquisition. Motion estimation could be introduced retrospectively using each FA dataset as a self-navigator (Dong et al., 2018b; Wang et al., 2018) or extra navigator acquisition with higher updating rates Gallichan and Marques (2017). Prospective motion correction methods can also be used (Maclaren et al., 2013; Todd et al., 2015) with less impact to the current reconstruction pipeline. Other effects such as eddy-current across different gradient echoes could be modeled in the future study.

To our knowledge, the 600 μm isotropic resolution dataset acquired at 7T is the highest resolution MWI that has been performed *in vivo* so far, and the line of Gennari observed in the MWF map preliminarily demonstrates the possibility of using MWF as a more specific measurement of myelin content in the cortex. However, the visualization of these detail structures using MWF is still unfavorable compared to single-pool T_1, and further evidence (e.g., histology) would be necessary to validate the reliability of using MWF to study cortical myelination. Moreover, the ill-conditioned nature of multi-compartment analysis requires much longer data acquisition than the single-pool model to achieve the same SNR level. More dot-like low MWF values can be observed under high spatial resolution, which could be noise-related errors in model fitting due to the lower image SNR. Hence, single-pool analysis is still more practical for high resolution imaging of the cortex even though it is less specific to myelin water content. Note that although MWF has been shown to have a good correlation with myelin density (Laule et al., 2006), it is still an indirect measure of the myelin content that is a parameter calculated from a biophysical model and should not be interpreted as a gold-standard measurement.

EPTI differentiates itself from other quantitative imaging approach such as MR fingerprinting (MRF) (Ma et al., 2013) through its seamless integration of continuous EPI-based readout and optimized spatiotemporal encoding to help achieve high acquisition efficiency. In addition, cutting-edge MWI models can be easily combined with EPTI to obtain more parameters of interest such as frequency offsets, since these models are developed based on more conventional sequences of which we can directly incorporate EPTI into. Although it is a challenge to directly apply such advanced MWI models to MRF, several studies have also been conducted recently to combine MRF with a multi-compartment dictionary matching for MWF estimation (Chen et al., 2019; Hamilton et al., 2016; Nagtegaal et al., 2020) showing promising results.

In this study, an extended complex GRE-MWI model with T_1 correction was used as an example of the application of vFA-EPTI for multi-compartment analysis. The proposed acquisition can also be applied to other GRE-MWI models (Nam et al., 2015b; Song et al., 2020; van Gelderen et al., 2012), and to single-pool quantitative mapping as we have shown in Fig. 9 and 10. Moreover, the EPTI acquisition with subspace reconstruction can be easily adopted to other types of sequence such as spin-echo or gradient-and-spin-echo (GRASE) (Oshio and Feinberg, 1991; Prasloski et al., 2012) sequence for T_2-based multi-compartment

analysis, or combined with preparation pulses to obtain additional information such as magnetization transfer contrast which is also related to myelin.

5. Conclusions

The proposed vFA EPTI method with joint multi-compartment subspace reconstruction achieved high acceleration with good accuracy, providing a powerful technique for multi-compartment analysis and microstructural imaging at high spatial resolution. Whole-brain MWF, proton density, multi-compartment T_1, T_2* maps can be acquired simultaneously in 5 min at 1.5 mm isotropic resolution and 24 min at 1 mm isotropic resolution at 3T. Moreover, high resolution data at 600 μm isotropic were acquired at 7T, demonstrating the potential of the proposed method for submillimeter GRE-MWI to study cortical myeloarchitecture *in vivo*.

Supplementary Material

Refer to Web version on PubMed Central for supplementary material.

Acknowledgment

This work was supported by the NIH NIBIB (R01-EB020613, R01-EB019437, R01-MH116173, R01-EB028797, P41-EB015896, and U01-EB025162) and the instrumentation Grants (S10-RR023401, S10-RR023043, and S10-RR019307). José P. Marques and Kwok-Shing Chan are supported by the Netherlands Organisation for Scientific Research (NWO) with project number FOM-N-31/16PR1056.

Funding

This work was supported by the NIH NIBIB (R01-EB020613, R01-EB019437, R01-MH116173, R01-EB028797, P41-EB015896, and U01-EB025162) and the instrumentation Grants (S10-RR023401, S10-RR023043, and S10-RR019307). José P. Marques and Kwok-Shing Chan are supported by the Netherlands Organisation for Scientific Research (NWO) with project number FOM-N-31/16PR1056.

References

Alonso-Ortiz E, Levesque IR. Paquin R. Pike GB. 2017. Field inhomogeneity correction for gradient echo myelin water fraction imaging. Magn. Reson. Med 78, 49–57. [PubMed: 27416957]

Alonso-Ortiz E, Levesque IR, Pike GB, 2018. Multi-gradient-echo myelin water fraction imaging: comparison to the multi-echo-spin-echo technique. Magn. Reson. Med 79, 1439–1446. [PubMed: 28656649]

Amunts K. Zilles K. 2015. Architectonic mapping of the human brain beyond Brodmann. Neuron 88, 1086–1107. [PubMed: 26687219]

Boyd S, Parikh N, Chu E, Peleato B, Eckstein J, 2011. Distributed Optimization and Statistical Learning Via the Alternating Direction Method of Multipliers. Now Publishers Inc.

Chan K, Marques J, 2019. Brain tissue multi-compartment relaxometry - an improved method for in vivo myelin water imaging. In: Proceedings of the 27th Annual Meeting of ISMRM 2019, p. 421.

Chan KS. Marques JP. 2020. Multi-compartment relaxometry and diffusion informed myelin water imaging - promises and challenges of new gradient echo myelin water imaging methods. Neuroimage 221, 117159. [PubMed: 32663644]

Chen Y, Chen MH. Baluyot KR, Potts TM. Jimenez J. Lin W, Consortium, U.U.B.C.P.. 2019. MR fingerprinting enables quantitative measures of brain tissue relaxation times and myelin water fraction in the first five years of life. Neuroimage 186, 782–793. [PubMed: 30472371]

Dong Z. Dai E. Wang F. Zhang Z. Ma X. Yuan C. Guo H. 2018a. Model-based reconstruction for simultaneous multislice and parallel imaging accelerated multishot diffusion tensor imaging. Med. Phys 45, 3196–3204. [PubMed: 29758101]

Dong Z. Wang F. Ma X. Dai E. Zhang Z. Guo H. 2018b. Motion-corrected k-space reconstruction for interleaved EPI diffusion imaging. Magn. Reson. Med 79, 1992–2002. [PubMed: 28771867]

Dong Z, Wang F, Reese TG, Bilgic B, Setsompop K, 2020. Echo planar time-resolved imaging with subspace reconstruction and optimized spatiotemporal encoding. Magn. Reson. Med 84, 2442–2455. [PubMed: 32333478]

Dong Z, Wang F, Reese TG, Manhard MK, Bilgic B, Wald LL, Guo H, Setsompop K, 2019. Tilted-CAIPI for highly accelerated distortion-free EPI with point spread function (PSF) encoding. Magn. Reson. Med 81, 377–392. [PubMed: 30229562]

Du YP, Chu R, Hwang D, Brown MS, Kleinschmidt-DeMasters BK, Singel D, Simon JH, 2007. Fast multislice mapping of the myelin water fraction using multi-compartment analysis of T2* decay at 3T: a preliminary postmortem study. Magn. Reson. Med 58, 865–870. [PubMed: 17969125]

Filippi M, Rocca MA, Ciccarelli O, De Stefano N, Evangelou N, Kappos L, Rovira A, Sastre-Garriga J, Tintorè M, Frederiksen JL, Gasperini C, 2016. MRI criteria for the diagnosis of multiple sclerosis: MAGNIMS consensus guidelines. Lancet Neurol. 15, 292–303. [PubMed: 26822746]

Fischl B, 2012. FreeSurfer.. Neuroimage. 62, 774–781. [PubMed: 22248573]

Gallichan D, Marques JP, 2017. Optimizing the acceleration and resolution of three-dimensional fat image navigators for high-resolution motion correction at 7T. Magn. Reson. Med 77, 547–558. [PubMed: 26877158]

Glasser MF, Van Essen DC, 2011. Mapping human cortical areas in vivo based on myelin content as revealed by T1- and T2-weighted MRI. J Neurosci 31, 11597–11616. [PubMed: 21832190]

Guo R, Zhao Y, Li Y, Li Y, Liang ZP, 2019. Simultaneous metabolic and functional imaging of the brain using SPICE. Magn. Reson. Med 82, 1993–2002. [PubMed: 31294487]

Guo R, Zhao Y, Li Y, Wang T, Li Y, Sutton B, Liang ZP, 2020. Simultaneous QSM and metabolic imaging of the brain using SPICE: further improvements in data acquisition and processing. Magn. Reson. Med 85, 970–977. [PubMed: 32810319]

Haast RA, Ivanov D, Formisano E, Uludag K, 2016. Reproducibility and reliability of quantitative and weighted T1 and T2(*) mapping for myelin-based cortical parcellation at 7 Tesla. Front. Neuroanat 10, 112. [PubMed: 27917112]

Hamilton JI, Deshmane A, Griswold M, Seiberlich N, 2016. MR fingerprinting with chemical exchange (MRF-X) for in vivo multi-compartment relaxation and exchange rate mapping. In: Proceedings of the 24th Annual Meeting of ISMRM 2016, p. 431.

Hanspach J, Nagel AM, Hensel B, Uder M, Koros L, Laun FB, 2021. Sample size estimation: Current practice and considerations for original investigations in MRI technical development studies. Magn. Reson. Med 85, 2109–2116. [PubMed: 33058265]

Hildebrand C, Remahl S, Persson H, Bjartmar C, 1993. Myelinated nerve fibres in the CNS. Prog. Neurobiol 40, 319–384. [PubMed: 8441812]

Kellner E, Dhital B, Kiselev VG, Reisert M, 2016. Gibbs-ringing artifact removal based on local subvoxel-shifts. Magn. Reson. Med 76, 1574–1581. [PubMed: 26745823]

Lam F, Liang ZP, 2014. A subspace approach to high-resolution spectroscopic imaging. Magn. Reson. Med 71, 1349–1357. [PubMed: 24496655]

Laule C, Kozlowski P, Leung E, Li DK, Mackay AL, Moore GR, 2008. Myelin water imaging of multiple sclerosis at 7 T: correlations with histopathology. Neuroimage 40, 1575–1580. [PubMed: 18321730]

Laule C, Leung E, Li DK, Traboulsee A, Paty D, MacKay A, Moore GR, 2006. Myelin water imaging in multiple sclerosis: quantitative correlations with histopathology. Mult Scler J 12, 747–753.

Lee D, Lee J, Lee J, Nam Y, 2018a. Single-scan z-shim method for reducing susceptibility artifacts in gradient echo myelin water imaging. Magn. Reson. Med 80, 1101–1109. [PubMed: 29479737]

Lee H, Nam Y, Lee HJ, Hsu JJ, Henry RG, Kim DH, 2018b. Improved three-dimensional multi-echo gradient echo based myelin water fraction mapping with phase related artifact correction. Neuroimage 169, 1–10. [PubMed: 29191477]

Li Y, Guo R, Zhao Y, Wang T, Meng Z, Li Y, Liang ZP, 2019. Rapid high-resolution simultaneous acquisition of metabolites, myelin water fractions, and tissue susceptibility of the whole brain using “SPICY” 1H-MRSI. In: Proceedings of the 27th Annual Meeting of ISMRM 2019, p. 946.

Liang Z-P, 2007. Spatiotemporal imagingwith partially separable functions. In: 2007 4th IEEE International Symposium on Biomedical Imaging: From Nano to Macro. Proc IEEE Int Symp Biomed Imaging, pp. 988–991.

Lustig M, Pauly JM, 2010. SPIRiT: Iterative self-consistent parallel imaging reconstruction from arbitrary k-space. Magn. Reson. Med 64, 457–471. [PubMed: 20665790]

Lutti A, Dick F, Sereno MI, Weiskopf N, 2014. Using high-resolution quantitative mapping of R1 as an index of cortical myelination. Neuroimage 93, 176–188. [PubMed: 23756203]

Ma D, Gulani V, Seiberlich N, Liu K, Sunshine JL, Duerk JL, Griswold MA, 2013. Magnetic resonance fingerprinting. Nature 495, 187–192. [PubMed: 23486058]

Mackay A, Whittall K, Adler J, Li D, Paty D, Graeb D, 1994. In vivo visualization of myelin water in brain by magnetic resonance. Magn. Reson. Med 31, 673–677. [PubMed: 8057820]

Maclaren J, Herbst M, Speck O, Zaitsev M, 2013. Prospective motion correction in brain imaging: a review. Magn. Reson. Med 69, 621–636. [PubMed: 22570274]

Malik SJ, Teixeira R, Hajnal JV, 2018. Extended phase graph formalism for systems with magnetization transfer and exchange. Magn. Reson. Med 80, 767–779. [PubMed: 29243295]

Marques JP, Gruetter R, 2013. Exploring cortical cytoarchitecture in high resolution R1 maps. In: Proceedings of the 21st Annual Meeting of ISMRM, p. 266.

Marques JP, Khabipova D, Gruetter R, 2017. Studying cyto and myeloarchitecture of the human cortex at ultra-high field with quantitative imaging: R1, R2(*) and magnetic susceptibility. Neuroimage 147, 152–163. [PubMed: 27939794]

Meng Z, Guo R, Li Y, Guan Y, Wang T, Zhao Y, Sutton B, Li Y, Liang ZP, 2020. Accelerating T2 mapping of the brain by integrating deep learning priors with low-rank and sparse modeling. Magn. Reson. Med 85, 1455–1467. [PubMed: 32989816]

Nagtegaal M, Koken P, Amthor T, Doneva M, 2020. Fast multi-component analysis using a joint sparsity constraint for MR fingerprinting. Magn. Reson. Med 83, 521–534. [PubMed: 31418918]

Nam Y, Kim DH, Lee J, 2015a. Physiological noise compensation in gradient-echo myelin water imaging. Neuroimage 120, 345–349. [PubMed: 26172308]

Nam Y, Lee J, Hwang D, Kim DH, 2015b. Improved estimation of myelin water fraction using complex model fitting. Neuroimage 116, 214–221. [PubMed: 25858448]

Oh S-H, Bilello M, Schindler M, Markowitz CE, Detre JA, Lee J, 2013. Direct visualization of short transverse relaxation time component (ViSTa). Neuroimage 83, 485–492. [PubMed: 23796545]

Ong F, Cheng JY, Lustig M, 2018. General phase regularized reconstruction using phase cycling. Magn. Reson. Med 80, 112–125. [PubMed: 29159989]

Oshio K, Feinberg DA, 1991. GRASE (gradient-and spin-echo) imaging: a novel fast MRI technique. Magn. Reson. Med 20, 344–349. [PubMed: 1775061]

Paus T, 2018. Imaging microstructure in the living human brain: a viewpoint. Neuroimage 182, 3–7. [PubMed: 29024791]

Peng X, Lam F, Li Y, Clifford B, Liang ZP, 2018. Simultaneous QSM and metabolic imaging of the brain using SPICE. Magn. Reson. Med 79, 13–21. [PubMed: 29067730]

Prasloski T, Rauscher A, MacKay AL, Hodgson M, Vavasour IM, Laule C, Madler B, 2012. Rapid whole cerebrum myelin water imaging using a 3D GRASE sequence. Neuroimage 63, 533–539. [PubMed: 22776448]

Sati P, van Gelderen P, Silva AC, Reich DS, Merkle H, de Zwart JA, Duyn JH, 2013. Micro-compartment specific T2* relaxation in the brain. Neuroimage 77, 268–278. [PubMed: 23528924]

Setsompop K, Fan Q, Stockmann J, Bilgic B, Huang S, Cauley SF, Nummenmaa A, Wang F, Rathi Y, Witzel T, Wald LL, 2018. High-resolution in vivo diffusion imaging of the human brain with generalized slice dithered enhanced resolution: Simultaneous multislice (gSlider-SMS). Magn. Reson. Med 79, 141–151. [PubMed: 28261904]

Shin HG, Oh SH, Fukunaga M, Nam Y, Lee D, Jung W, Jo M, Ji S, Choi JY, Lee J, 2019. Advances in gradient echo myelin water imaging at 3T and 7T. Neuroimage 188, 835–844. [PubMed: 30476624]

Song JE, Shin J, Lee H, Lee HJ, Moon WJ, Kim DH, 2020. Blind source separation for myelin water fraction mapping using multi-echo gradient echo imaging. IEEE Trans. Med. Imaging 39, 2235–2245. [PubMed: 31976881]

Sumpf TJ, Uecker M, Boretius S, Frahm J, 2011. Model-based nonlinear inverse reconstruction for T2 mapping using highly undersampled spin-echo MRI. J. Magn. Reson. Imaging 34, 420–428. [PubMed: 21780234]

Tamir JI, Taviani V, Alley MT, Perkins BC, Hart L, O'Brien K, Wishah F, Sandberg JK, Anderson MJ, Turek JS, Willke TL, Lustig M, Vasanawala SS, 2019. Targeted rapid knee MRI exam using T2 shuffling. J. Magn. Reson. Imaging 49, e195–e204. [PubMed: 30637847]

Todd N, Josephs O, Callaghan MF, Lutti A, Weiskopf N, 2015. Prospective motion correction of 3D echo-planar imaging data for functional MRI using optical tracking. Neuroimage 113, 1–12. [PubMed: 25783205]

van Gelderen P, de Zwart JA, Lee J, Sati P, Reich DS, Duyn JH, 2012. Nonexponential T(2) decay in white matter. Magn. Reson. Med 67, 110–117. [PubMed: 21630352]

Wang F, Bilgic B, Dong Z, Manhard MK, Ohringer N, Zhao B, Haskell M, Cauley SF, Fan Q, Witzel T, Adalsteinsson E, Wald LL, Setsompop K, 2018. Motion-robust sub-millimeter isotropic diffusion imaging through motion corrected generalized slice dithered enhanced resolution (MC-gSlider) acquisition. Magn. Reson. Med 80, 1891–1906. [PubMed: 29607548]

Wang F, Dong Z, Reese TG, Bilgic B, Katherine Manhard M, Chen J, Polimeni JR, Wald LL, Setsompop K, 2019a. Echo planar time-resolved imaging (EPTI). Magn. Reson. Med 81, 3599–3615. [PubMed: 30714198]

Wang F, Dong Z, Reese TG, Wald LL, Setsompop K, 2019b. 3D-EPTI for Ultra-fast Multi-contrast and Quantitative Imaging. In: Proceedings of the 27th Annual Meeting of ISMRM 2019, p. 944.

Wang Y, Wu C, Caprariello AV, Somoza E, Zhu W, Wang C, Miller RH, 2009. In vivo quantification of myelin changes in the vertebrate nervous system. J. Neurosci 29, 14663–14669. [PubMed: 19923299]

Webb S, Munro CA, Midha R, Stanisz GJ, 2003. Is multicomponent T2 a good measure of myelin content in peripheral nerve? Magn. Reson. Med 49, 638–645. [PubMed: 12652534]

Weiskopf N, Mohammadi S, Lutti A, Callaghan MF, 2015. Advances in MRI-based computational neuroanatomy: from morphometry to in-vivo histology. Curr. Opin. Neurol 28, 313–322. [PubMed: 26132532]

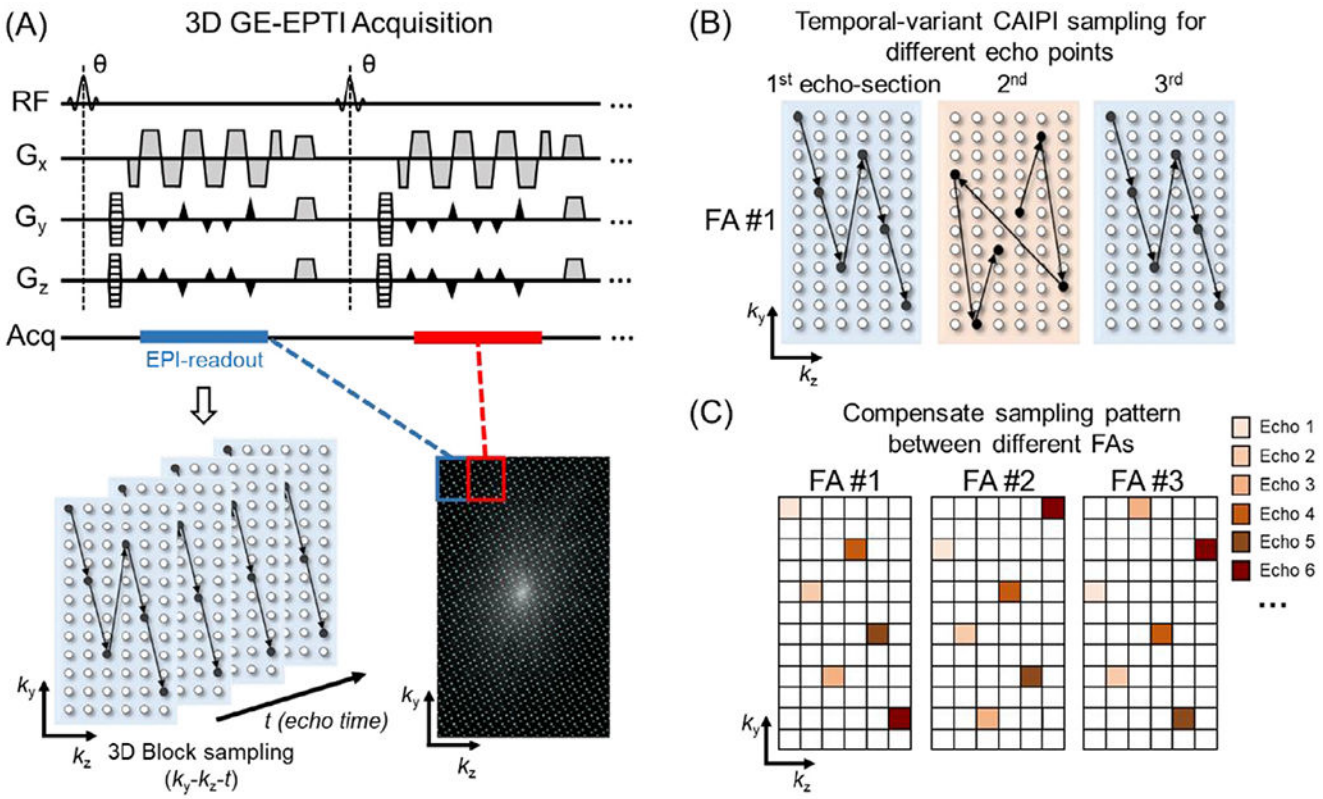

Fig. 1.

(A) The diagram of 3D GE-EPTI sequence, and the graphic illustration of the block-wise sampling of each EPTI readout in the k_y-k_z-t space. Readout dimension (k_x) is omitted in all the figures. (B) Illustration of the temporal-variant CAIPI sampling, where odd and even echo-sections have different sampling patterns to create complementary sampling of k_y-k_z encodes over time. (C) The sampling pattern in each block for different FAs are also designed to be complementary for better reconstruction accuracy.

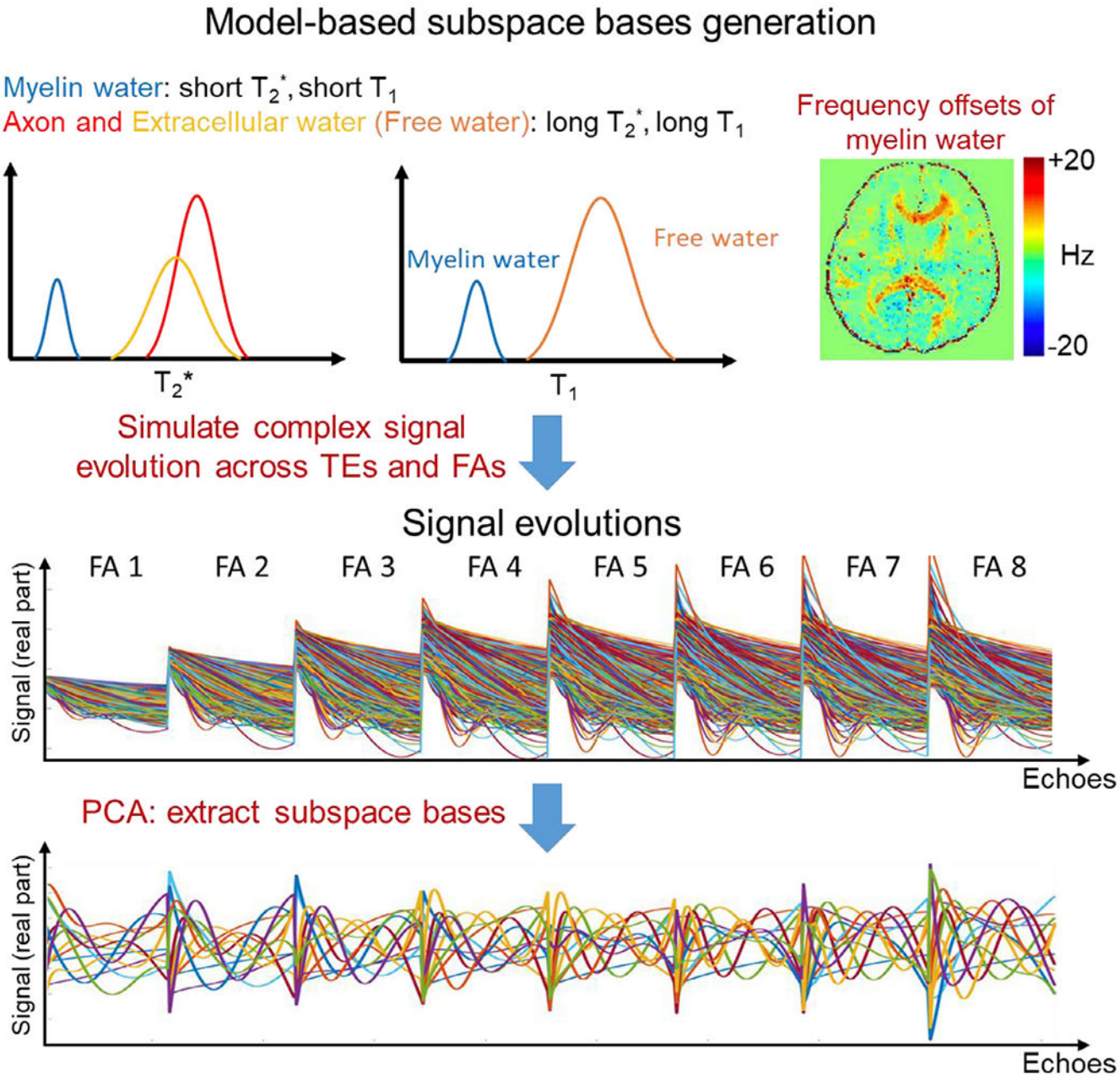

Fig. 2.

The graphic illustration of the subspace basis generation for vFA-EPTI using multi-compartment relaxometry (MCR) model. In the MCR model, three water pools: myelin water (MW), axon water (AX) and extracellular water (EX) are modeled to have different amplitudes, T_2*, and frequency offsets. For longitudinal relaxation modeling, two water pools are assumed: free water (axon and extracellular water) pool and myelin sheath pool. Using the MCR model and a wide range of parameters, complex signal evolutions across different TEs and FAs of the vFA multi-echo acquisition can be simulated, and PCA is performed on the simulated signals to extract the complex subspace bases.

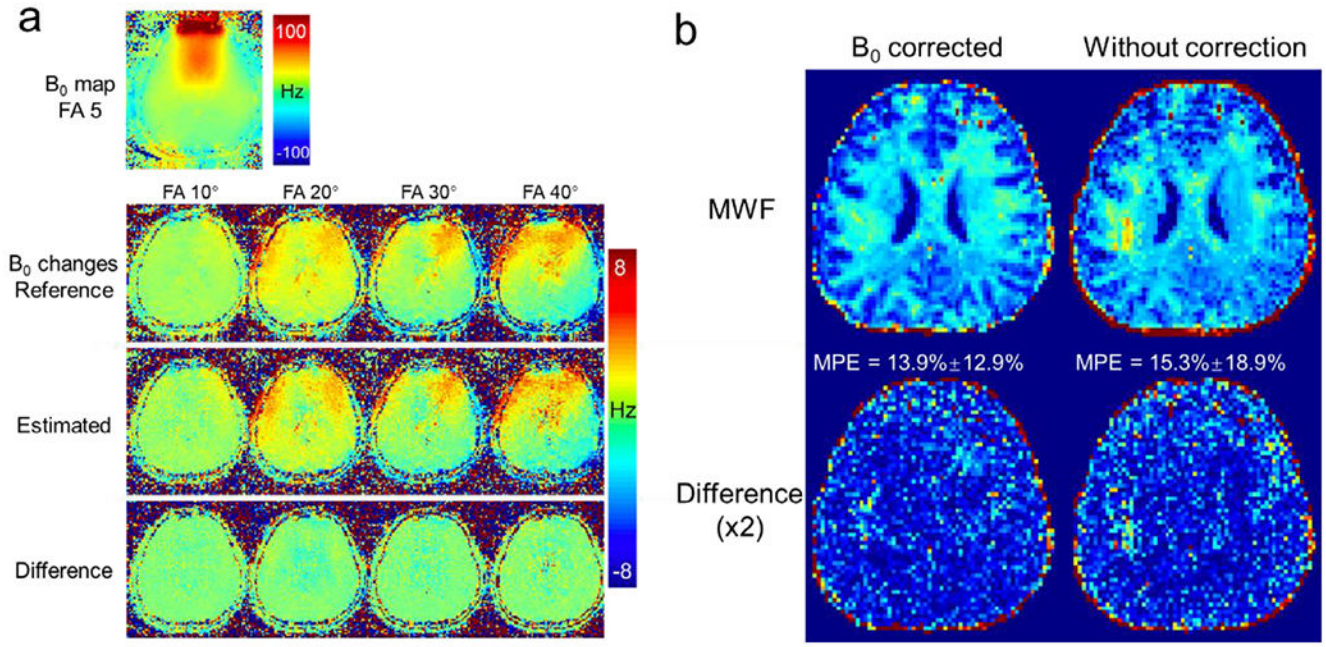

Fig. 3.

Evaluation of the estimated changes in the B_0 field across different FA acquisitions (Experiment 1). (**a**) The top image shows the B_0 map at FA = 5°. The B_0 changes relative to the B_0 map at FA = 5° calculated from the fully-sampled data (first row), and the estimated B_0 changes from the 26 × retrospectively undersampled vFA-EPTI data (second row) are similar with small differences (third row). (**b**) Comparison of the accuracy of MWF estimation with and without B_0 change correction in the joint subspace reconstruction. The difference maps are magnified by a factor of 2. MPE: mean percentage error.

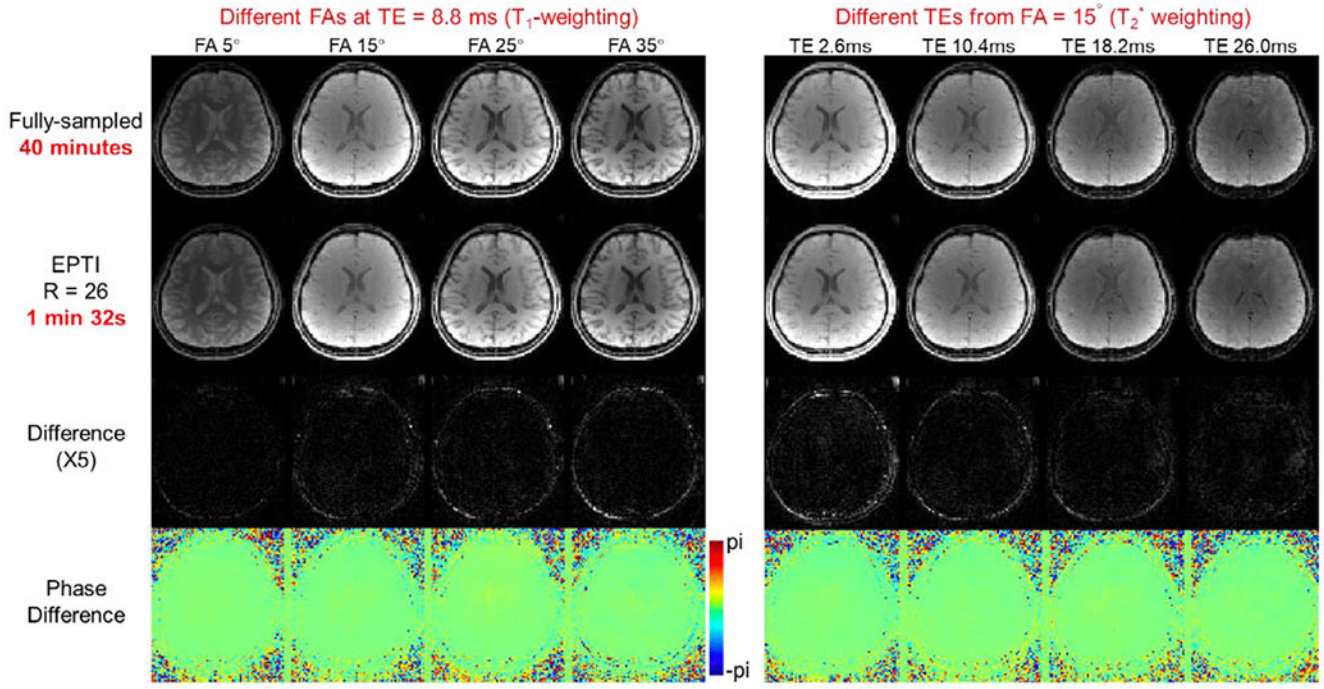

Fig. 4.

Comparison of the fully-sampled reference data and the reconstructed vFA-EPTI images at $R = 26$ (Experiment 1). The magnitude images, the difference maps of the magnitude (magnified by × 5) and the phase at four representative FAs and TEs are shown. The differences between the reconstructed images and the reference images are small and mostly noise like. However, the acquisition time is significantly reduced from 40 min to 1 min and 32 s by using the proposed vFA-EPTI acquisition.

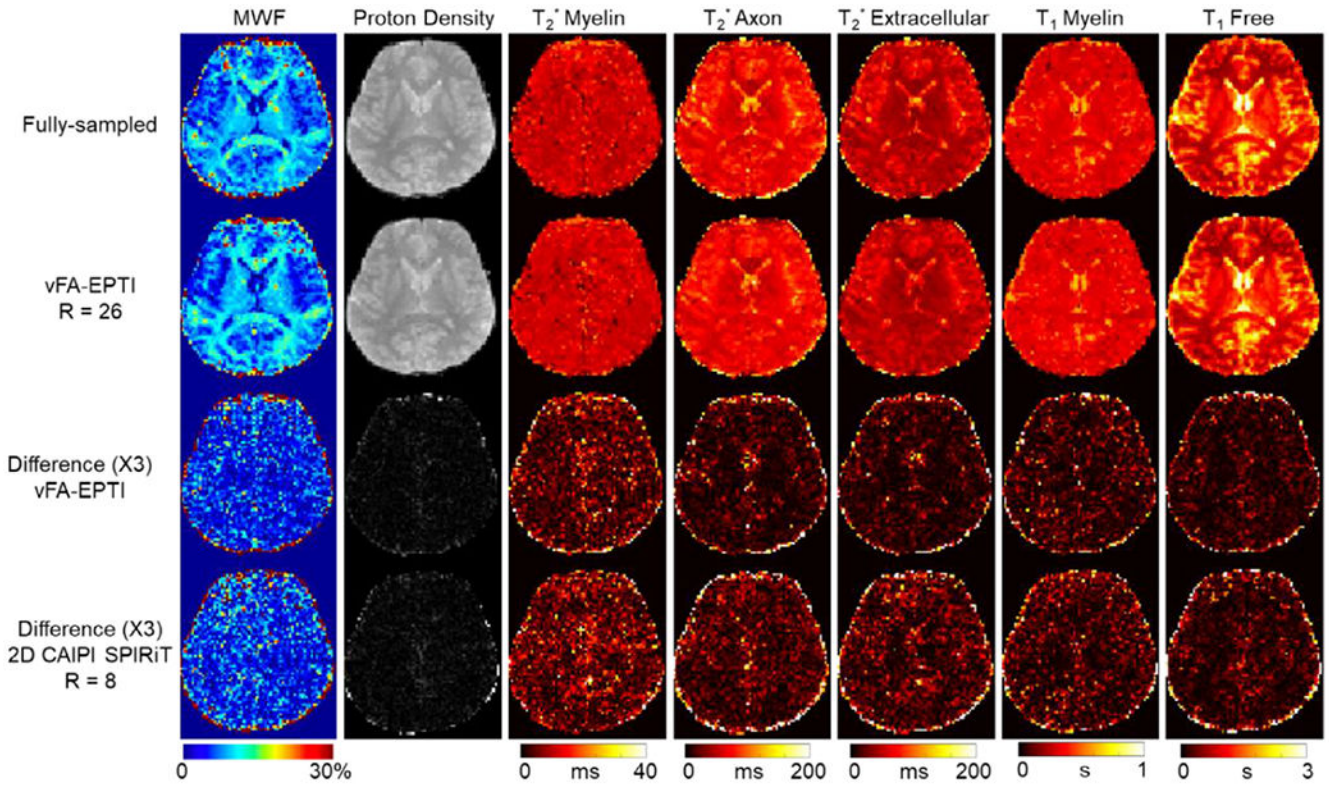

Fig. 5.

The estimated quantitative parameters from the fully-sampled reference data and vFA-EPTI ($R = 26$) using the MCR model (Experiment 1). The difference maps (magnified by a factor of × 3) were calculated using the fully-sampled data as the gold-standard. MWF and the other quantitative parameters estimated from vFA-EPTI appear to have lower errors than 2D CAIPI sampling with SPIRiT ($R = 8$), even when vFA-EPTI used a three times higher acceleration factor.

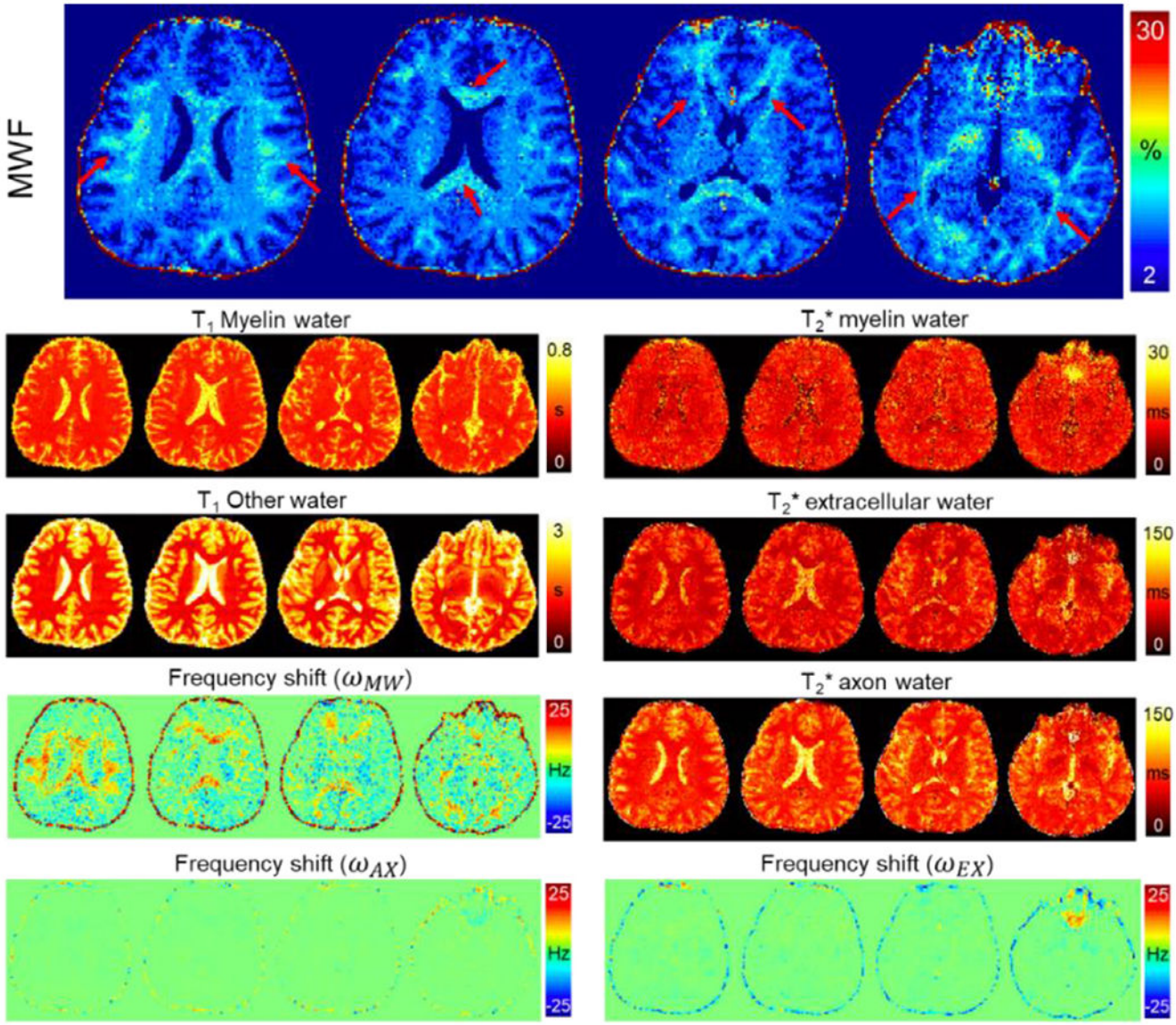

Fig. 6.

The estimated MWF and multi-compartment quantitative parameters of the 5 min 1.5 mm isotropic acquisition using vFA-EPTI at $R = 26$ at 3T (Experiment 2). The estimated MWF in the white-matter areas show relatively higher values than in the gray matter, and the highly-myelinated fiber bundles including the cingulum, genu and splenium of corpus callosum, corona radiata and optic radiation (red arrows) can be observed in the MWF maps.

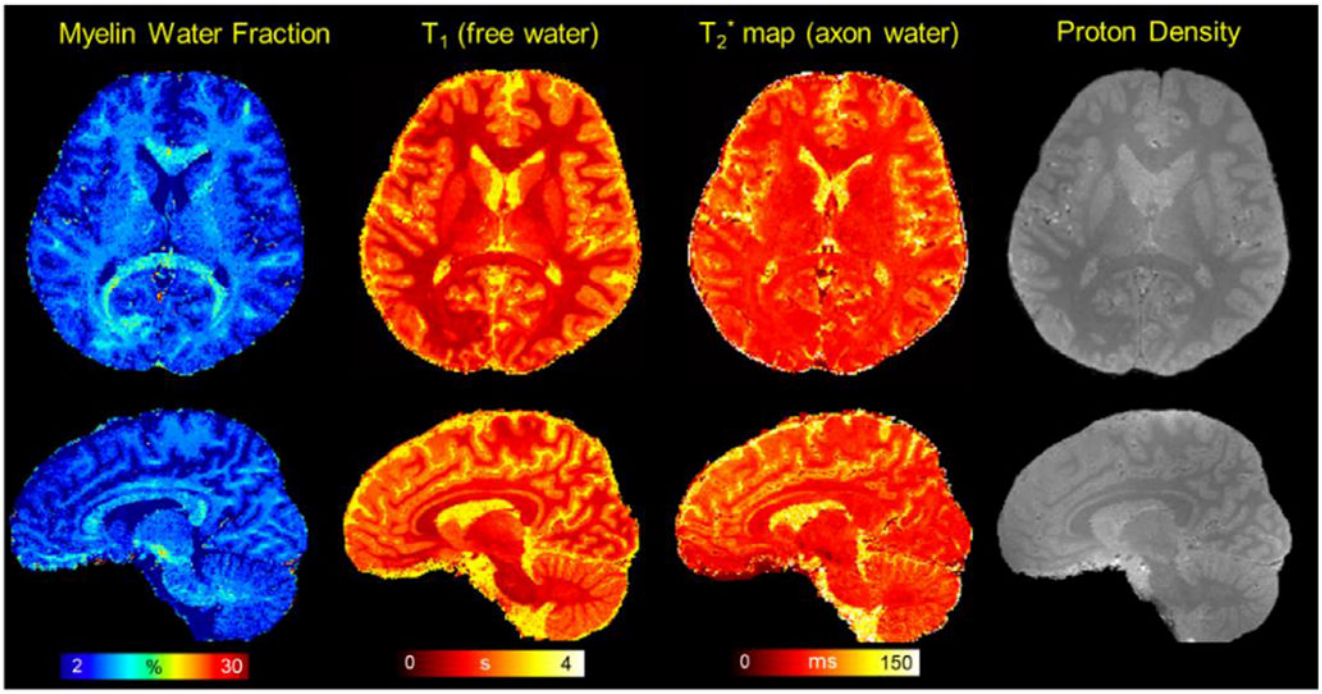

Fig. 7.

Representative axial and sagittal images of the estimated MWF, T_1 of free water, T_2* of axon water and total proton density acquired at 1 mm isotropic resolution in 24 min at 3T with $R = 13$ (Experiment 3). All the images show good quality at this high spatial resolution on 3T. The delineation of the fiber bundles (e.g., corpus callosum, optic radiation) in the MWF maps are improved compared to the results from the 1.5 mm dataset due to the increased resolution, and the gray-white mater boundary is clearly delineated in the T_1 map of free water.

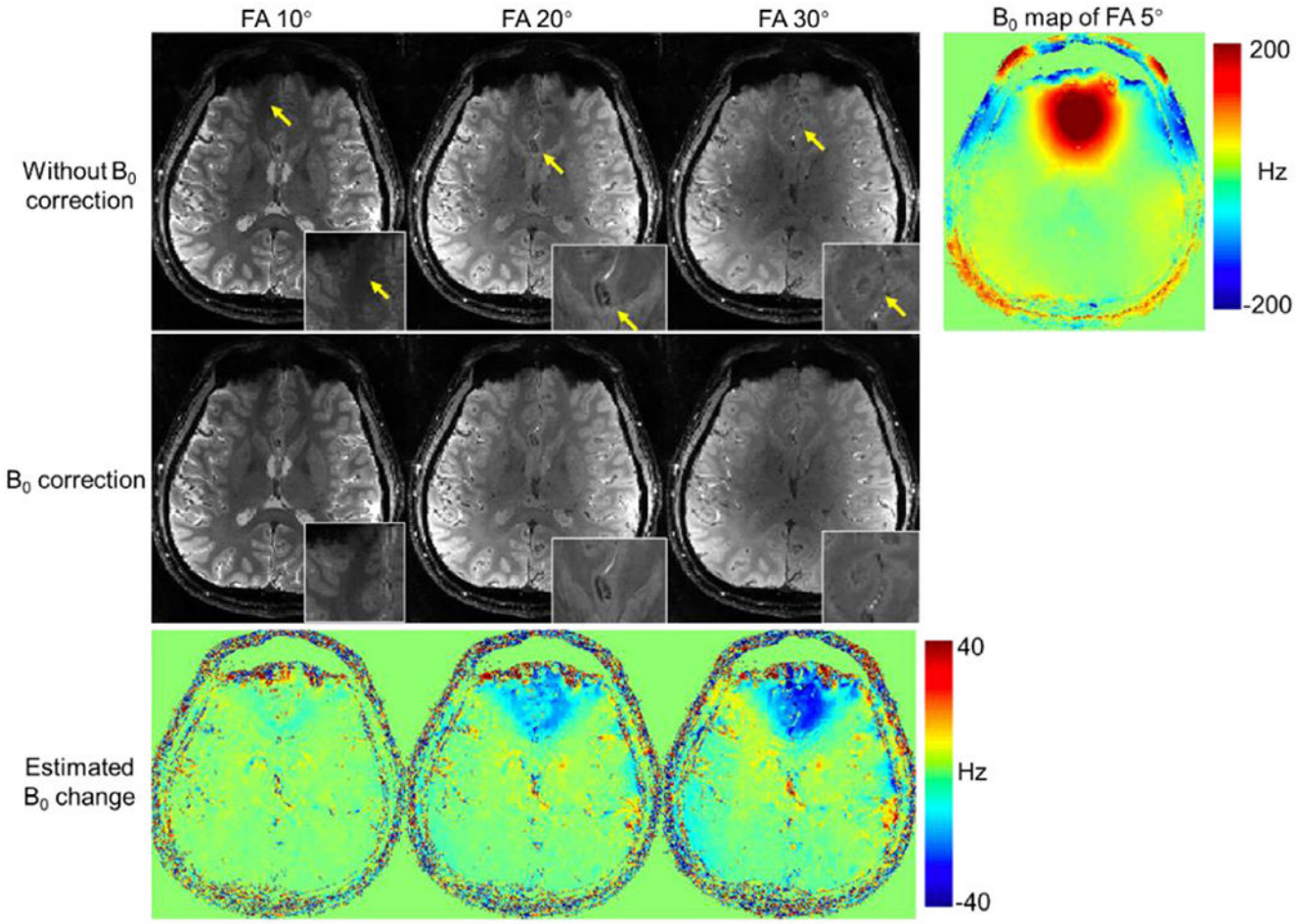

Fig. 8.

Evaluation of the B_0 change estimation and correction in the 600 μm 7T experiment (Experiment 4). The B_0 off-resonance (right figure) and changes across FAs (bottom row) are much larger at 7T when compared to those at 3T (Fig. 3). The uncorrected joint subspace reconstruction shows noticeable artifacts in the zoomed-in areas (top row, yellow arrows). After incorporating the B_0 changes into the joint reconstruction, these artifacts are well mitigated, leading to improved accuracy of the images.

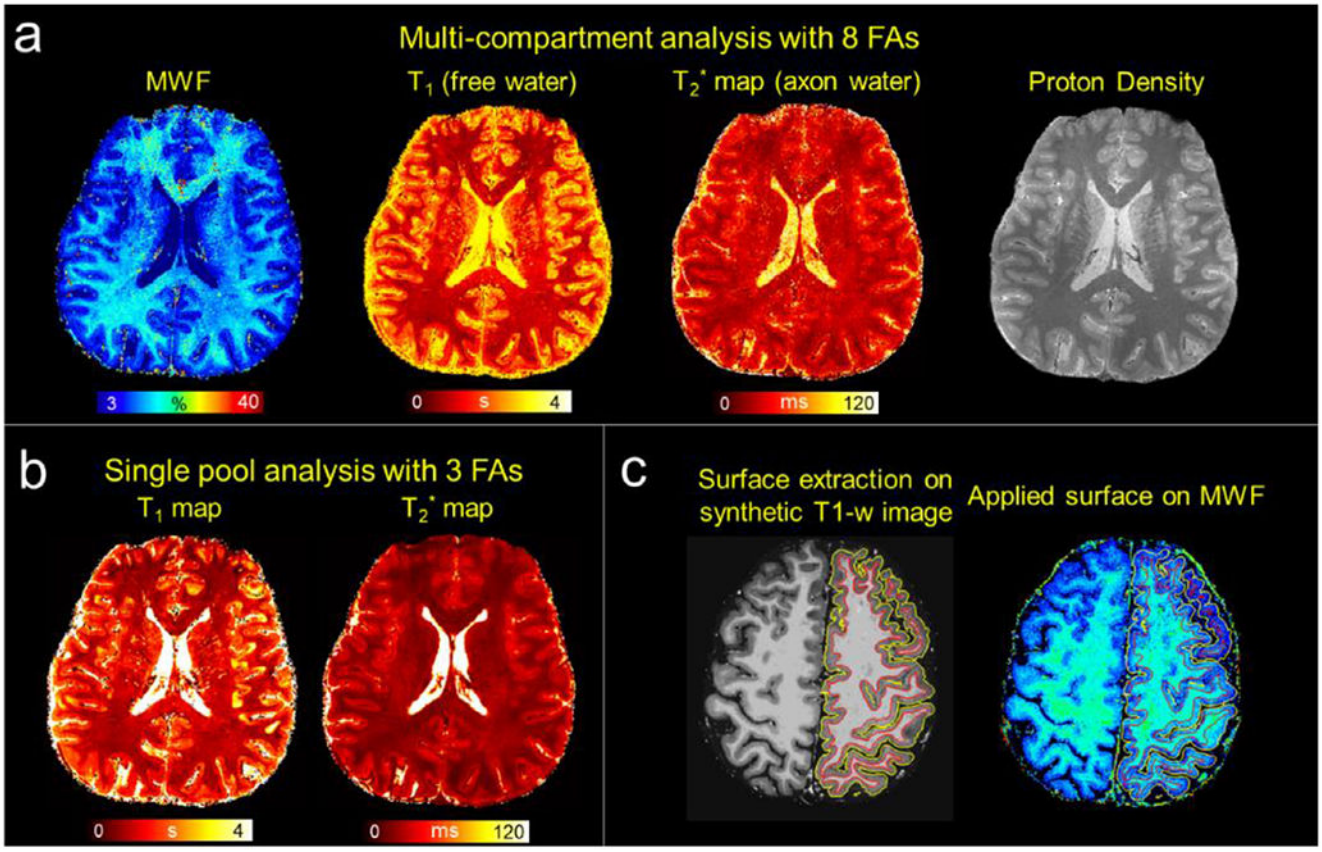

Fig. 9.

Results of the 600-μm 7T experiment (Experiment 4). (a) Quantitative maps estimated using multi-compartment analysis with 8 FAs. (b) T_1 and T_2* map estimated using single pool analysis with only 3 FAs. (c) Surface extraction was performed on the synthesized T_1 -weighted images which was then applied to the quantitative maps.

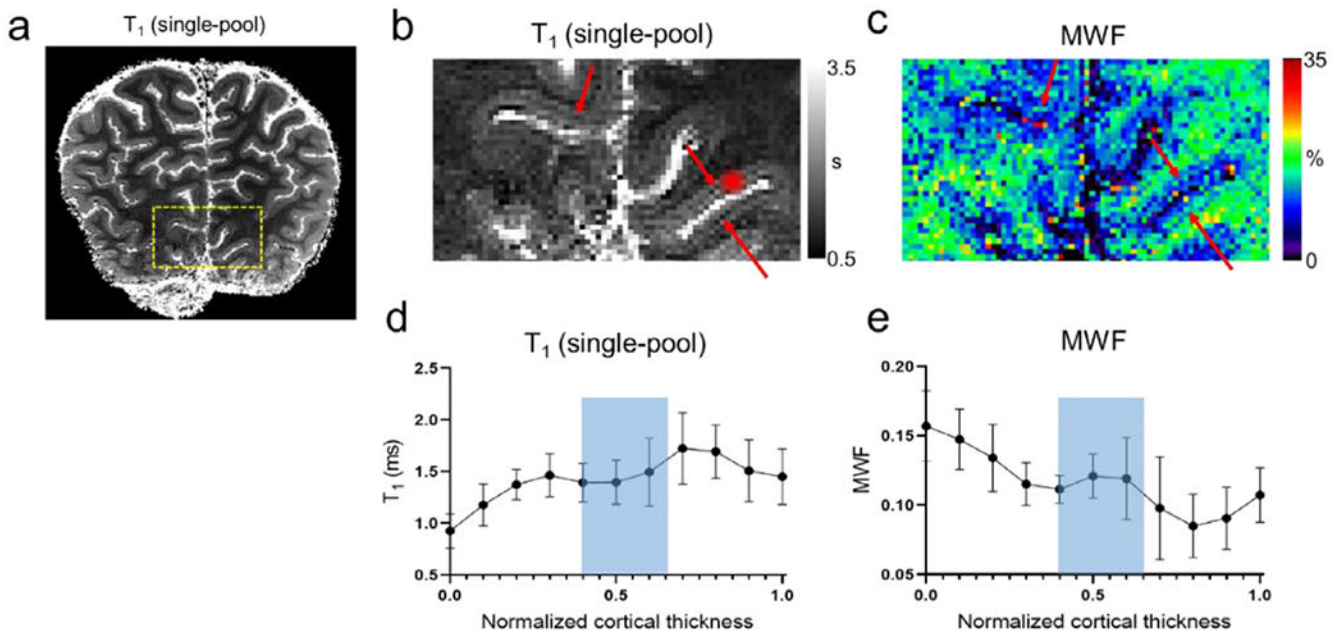

Fig. 10.

The zoomed-in T_1 (b) and MWF (c) maps in the calcarine sulcus area shown in a dashed square (a). The line of Gennari can be seen as hypo-intense bands in the middle of cortical thickness (red arrows in (b)) in the T_1 map, and as green bands with higher values (red arrows in (c)) in the MWF map. The values of T_1 and MWF at a sampled area (red circle in b) across different cortical depths are plotted in (d) and (e). Error bars are the standard deviations over all profiles for each location. In the middle cortical depth region (blue window), T_1 shows a decreased value and MWF shows an increased value that correlate with the higher myelination level of the line of Gennari.